Mice deficient in *Epg5* exhibit selective neuronal vulnerability to degeneration

Hongyu Zhao,[1,4] Yan G. Zhao,[2,4] Xingwei Wang,[2,4] Lanjun Xu,[2,4] Lin Miao,[4] Du Feng,[5] Quan Chen,[3] Attila L. Kovács,[6] Dongsheng Fan,[7] and Hong Zhang[2]

[1]College of Life Sciences, China Agricultural University, Beijing 100083, China
[2]State Key Laboratory of Biomacromolecules, Institute of Biophysics; and [3]State Key Laboratory of Biomembrane and Membrane Biotechnology, Institute of Zoology; Chinese Academy of Sciences, Beijing 100101, China
[4]National Institute of Biological Sciences, Beijing 102206, China
[5]Institute of Neurology, Affiliated Hospital of Guangdong Medical College, Zhanjiang 524001, China
[6]Department of Anatomy, Cell, and Developmental Biology, Eötvös Loránd University, Budapest H-1117, Hungary
[7]Department of Neurology, Peking University Third Hospital, Beijing 100191, China

The molecular mechanism underlying the selective vulnerability of certain neuronal populations associated with neurodegenerative diseases remains poorly understood. Basal autophagy is important for maintaining axonal homeostasis and preventing neurodegeneration. In this paper, we demonstrate that mice deficient in the metazoan-specific autophagy gene *Epg5/epg-5* exhibit selective damage of cortical layer 5 pyramidal neurons and spinal cord motor neurons. Pathologically, *Epg5* knockout mice suffered muscle denervation, myofiber atrophy, late-onset progressive hindquarter paralysis, and dramatically reduced survival, recapitulating key features of amyotrophic lateral sclerosis (ALS). *Epg5* deficiency impaired autophagic flux by blocking the maturation of autophagosomes into degradative autolysosomes, leading to accumulation of p62 aggregates and ubiquitin-positive inclusions in neurons and glial cells. *Epg5* knockdown also impaired endocytic trafficking. Our study establishes *Epg5*-deficient mice as a model for investigating the pathogenesis of ALS and indicates that dysfunction of the autophagic–endolysosomal system causes selective damage of neurons associated with neurodegenerative diseases.

Introduction

Autophagy is a degradation system involving the enclosure of cytosolic components in a double-membrane autophagosome and their subsequent delivery to the vacuole/lysosome for degradation (Nakatogawa et al., 2009). In yeast, autophagosomes directly fuse with the vacuole, whereas nascent autophagosomes in higher eukaryotes undergo maturation processes, including fusion with endosomes, before fusion with lysosomes to produce degradative autolysosomes (Longatti and Tooze, 2009). The more elaborate autophagic machinery in higher eukaryotes involves highly conserved Atg (autophagy related) proteins, factors involved in the endolysosomal pathway, and also metazoan-specific autophagy proteins (Longatti and Tooze, 2009; Tian et al., 2010).

Basal autophagy removes misfolded and toxic aggregate-prone proteins and damaged organelles (Levine and Kroemer, 2008). Neural-specific depletion of genes essential for autophagosome formation, including *Atg5*, *Atg7*, and *Ei24*, causes accumulation of p62 aggregates and ubiquitin-positive inclusions and leads to axonal degeneration and massive nonselective neuronal loss (Hara et al., 2006; Komatsu et al., 2006; Zhao et al., 2012). In contrast, neurodegenerative diseases, such as amyotrophic lateral sclerosis (ALS), Huntington's disease, and Alzheimer's disease, involve selective damage of certain neuronal populations (Hardy and Gwinn-Hardy, 1998). For example, ALS is characterized by the selective loss of motor neurons in cortical layer 5 and in the spinal cord and manifests as muscle weakness,

H. Zhao, Y.G. Zhao, and X. Wang contributed equally to this paper.

Correspondence to Yan G. Zhao: izhaoyan@moon.ibp.ac.cn; or Hong Zhang: hongzhang@sun5.ibp.ac.cn

Abbreviations used in this paper: ALS, amyotrophic lateral sclerosis; AMC, aminomethylcoumarin; CMAP, compound muscle action potential; DCN, deep cerebellar nuclei; EGFR, EGF receptor; GFAP, glial fibrillary acidic protein; H&E, hematoxylin and eosin; MEF, mouse embryonic fibroblast; MUAP, motor unit action potential; NS, nonsense.

The Rockefeller University Press $30.00
J. Cell Biol. Vol. 200 No. 6 731–741
www.jcb.org/cgi/doi/10.1083/jcb.201211014

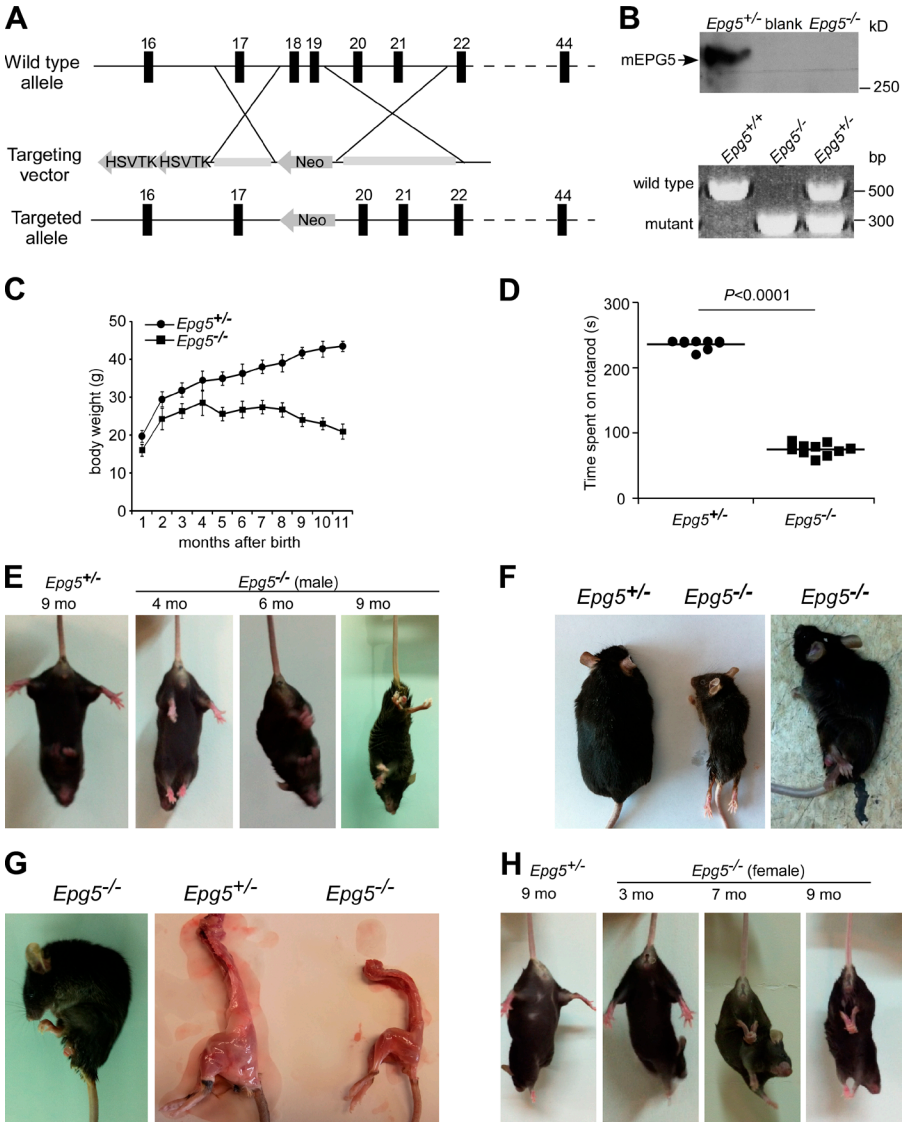

Figure 1. ***Epg5*$^{-/-}$ mice show motor deficits.** (A) Scheme for generating *Epg5* knockout mice. HSVTK, herpes simplex virus thymidine kinase; Neo, neomycin. (B) Epg5 protein and the wild-type copy of *Epg5* are absent in *Epg5*$^{-/-}$ mice. There is an intervening lane between *Epg5*$^{+/-}$ and *Epg5*$^{-/-}$ lanes in the Western blot. (C) Body weight curves of *Epg5*$^{+/-}$ and *Epg5*$^{-/-}$ males. Means ± SEM of 12 mice are shown. (D) Time spent on a rotarod. The horizontal lines indicate mean times. (E) *Epg5*$^{-/-}$ males show gradually worsening limb-clasping reflexes. (F) The hindquarters of *Epg5*$^{-/-}$ mice are completely paralyzed at 10 mo of age. (G) Spinal deformation in an *Epg5*$^{-/-}$ male at 10 mo of age. (H) *Epg5*$^{-/-}$ females gradually develop the limb-clasping phenotype.

muscle atrophy, and late onset paralysis (Boillée et al., 2006; Pasinelli and Brown, 2006). More than 16 causative genes have been linked to ALS, including *SOD1*, encoding Cu/Zn superoxide dismutase, and *TARDBP*, encoding the RNA-binding protein TDP-43 (Neumann et al., 2006; Ferraiuolo et al., 2011). Autophagic vacuoles accumulate in the spinal cord motor neurons of sporadic ALS patients and also in mutant *Sod1* ALS model mice (Zhang et al., 2011; Otomo et al., 2012). The role of autophagy in the pathogenesis of ALS and in specific motor neuron degeneration has not been determined by loss-of-function approaches.

Genetic screens in *Caenorhabditis elegans* have identified *epg-5* as a metazoan-specific autophagy gene that acts at a genetic step downstream of all known *Atg* genes (Tian et al., 2010; Lu et al., 2011). Here, we demonstrate that mice deficient in *Epg5* recapitulate key neuropathological characteristics of ALS. *Epg5* is required for autophagosome maturation and endocytic trafficking. Our results suggest that accumulation of autophagic vacuoles causes selective degeneration of certain neuronal populations.

Results and discussion

Epg5$^{-/-}$ mice develop behavioral and motor abnormalities

We generated *Epg5* knockout mice as shown in Fig. 1 (A and B). *Epg5* heterozygous mice (*Epg5*$^{+/-}$) had no noticeable pathological defects over a 2-yr period. *Epg5* homozygous offspring (*Epg5*$^{-/-}$) were born at Mendelian frequency and appeared normal at birth but showed growth retardation and reduced survival (Fig. 1 C). *Epg5*$^{-/-}$ mice developed progressive behavioral and motor deficits. They showed poor motor coordination in a rotarod test at 4 mo (Fig. 1 D) and gradually exhibited limb-clasping reflexes (Fig. 1 E). The hindquarters became completely paralyzed and stiff in *Epg5*$^{-/-}$ males at 10 mo, accompanied by poor grooming, rough coat, flank muscle wasting, and notable kyphosis (Fig. 1, F and G). *Epg5*$^{-/-}$ males started to die by 10 mo after birth. *Epg5*$^{-/-}$ females were similarly affected, but the phenotype occurred later than in males (Fig. 1 H). Three out of four females died at 8–10 mo with slight hind-limb paralysis and muscle wasting, and one female survived to 12 mo and showed complete hind-limb paralysis.

Selective vulnerability of cerebral cortex layer 5 and hippocampal pyramidal neurons and spinal cord motor neurons in *Epg5*$^{-/-}$ mice

Histological analyses were performed on cerebrum, cerebellum, and spinal cord sections from control and mutant mice at 10 mo of age. In *Epg5*$^{-/-}$ males, total brain size was comparable to controls. The number of neurons in cortical layers 1–4 remained unchanged (Fig. S1 A), but the number of pyramidal neurons in layer 5 of the motor and sensory cortices was reduced by 28 and 37%, respectively (Figs. 2, A and B; and S1 B). The thickness and cell number of the hippocampal pyramidal cell layer was reduced (Fig. 2, C and D). The pattern of nerve fibers in the alveus of the hippocampus was slightly irregular (Fig. S1 C).

Epg5$^{-/-}$ mutant cerebella appeared normal: the size, foliation, and fissuration were comparable with controls as was the thickness of the molecular layer (Fig. 2, E and F). Purkinje cell numbers and the distribution of Purkinje cell axon terminals in the deep cerebellar nuclei (DCN) of *Epg5*-deficient mice were similar to controls (Figs. 2, G and H; and S1 D). *Epg5*$^{-/-}$ mice had fewer motor neurons in the anterior horn of the cervical, thoracic, and lumbar spinal cord (Fig. 2, I and J). Many of the remaining motor neurons were pyknotic (Fig. 2 I). The number of interneurons was normal (Fig. 2 K). Eosinophilic spheroids accumulated in the dorsal corticospinal tract of the cervical, thoracic, and lumbar spinal cord in *Epg5*$^{-/-}$ mice (Fig. 2 L). The eosinophilic spheroids were stained by the axon marker β-tubulin III and were surrounded by discontinuous myelin basic protein–stained myelin (Fig. 2 M), indicating that these spheroids were swollen degenerating axons. Ultrastructurally, *Epg5*$^{-/-}$ mice brains contain many atrophic motor neurons in the cortex (Fig. S1 F). *Epg5*$^{-/-}$ mice also showed many degenerating axons and swollen mitochondria in the spinal cord (Figs. 2 N and S1 E). Expression of the glial marker glial fibrillary acidic protein (GFAP) increased in various regions of the cerebrum, cerebellum, and spinal cord of mutant mice compared with control littermates, indicating that *Epg5*$^{-/-}$ mice exhibit reactive astrogliosis (Figs. 2, O and P; and S1, G and H).

Accumulation of p62 aggregates and ubiquitin-positive inclusions in *Epg5*- deficient mice

We next examined whether *Epg5* is essential for basal autophagy activity by examining the level and distribution of p62, polyubiquitinated proteins, and LC3 (mammalian Atg8 homologue; Mizushima et al., 2010). Brain and spinal cord extracts from *Epg5*$^{-/-}$ mice at 10 mo showed dramatic accumulation of p62, high molecular mass polyubiquitinated proteins, and LC3-II, a lipidated form of LC3 that associates with autophagic vacuoles (Fig. 3, A and B). *p62* mRNA levels and proteasome activity were comparable in controls and mutants (Fig. S1, I and J). Cytoplasmic p62 aggregates and ubiquitin-positive inclusions accumulated in various regions of the cerebrum, cerebellum, and spinal cord of *Epg5*$^{-/-}$ but not *Epg5*$^{+/-}$ mice (Figs. 3 C and S1, K–N). p62 colocalized with neuronal nuclei–labeled neurons and anti-CNPase (2′,3′-cyclic-nucleotide 3′-phosphodiesterase)–labeled oligodendrocytes but absent from GFAP-stained astroglia (Fig. 3, D–F). Ubiquitin-positive inclusions colocalized with p62 aggregates, but they were fewer in number than p62 aggregates (Figs. 3 C and S1 N). LC3 was diffusely localized with very few puncta detected in wild-type brain and spinal cord (Fig. S1, P–R). In *Epg5*$^{-/-}$ mice, LC3 foci dramatically accumulated in SMI 32–labeled motor neurons and oligodendroglia (Fig. S1 P). LC3 immunoreactivity largely colocalized with p62 aggregates (Fig. S1, O, Q, and R). Thus, *Epg5* deficiency impairs autophagic flux, leading to accumulation of LC3 puncta, p62 aggregates, and ubiquitin-positive inclusions in neurons and glial cells.

Epg5 deficiency causes accumulation of cytoplasmic TDP-43 aggregates

Accumulation of cytoplasmic TDP-43 aggregates in vulnerable neurons is a common feature of ALS and frontotemporal lobar degeneration (Neumann et al., 2006). In *Epg5*$^{+/-}$ mice, TDP-43 showed nuclear staining in neurons in various regions of brain and spinal cord (Fig. 3 G). However, a large number of TDP-43 aggregates accumulated in the cytoplasm in motor neurons in the spinal cord and the fifth layer of cortices and, to a lesser extent, in neurons in other brain regions of *Epg5*$^{-/-}$ mice (Figs. 3, G and H; and S1 T). Protein levels of TDP-43 remained unchanged in mutant mice (Fig. S1 S). Cytoplasmic TDP-43 aggregates were absent in motor neurons in *Ei24*-deficient mice (Fig. S1 U).

Epg5-deficient mice show muscle denervation and myofiber degeneration

Electromyography was performed to determine whether *Epg5* deficiency causes muscle denervation, characteristic of the early stage of motor neuron diseases (Boillée et al., 2006). Fibrillation and positive sharp waves were found in the resting gastrocnemius (lower hind limb) muscle of 3-mo-old *Epg5*$^{-/-}$ mice (presymptomatic), indicative of active denervation of muscle fibers (Fig. 4, A and B). At 7 mo (early symptomatic), the duration of the motor unit action potential (MUAP) at moderate contractions increased 44% in *Epg5*$^{-/-}$ mice compared with controls, indicating reinnervation of denervated muscle fibers by the sprout from relatively normal axons. At 10 mo, MUAP duration increased 78% in *Epg5*$^{-/-}$ mice with occasional high-amplitude and long-duration action potentials (Fig. 4 C), but no fibrillation or positive sharp waves were found, indicating no obvious active denervation in end-stage *Epg5*$^{-/-}$ mice. Moreover, the bicipital (upper forelimb) muscle started to suffer denervation changes at 10 mo, indicated by the appearance of positive sharp waves. The evoked motor response (compound muscle action potential [CMAP]) of the gastrocnemius muscle elicited by distal stimulation of the sciatic nerve in *Epg5*$^{-/-}$ mice at 7 and 10 mo exhibited increased latency and decreased amplitude (Fig. S2 A), indicating axonal degeneration. Thus, *Epg5*$^{-/-}$ mice showed neurogenic muscle damage progressing from hind limb to forelimb.

Histological analysis of the gastrocnemius muscle of *Epg5*$^{-/-}$ mice at 10 mo revealed myofiber degeneration, including

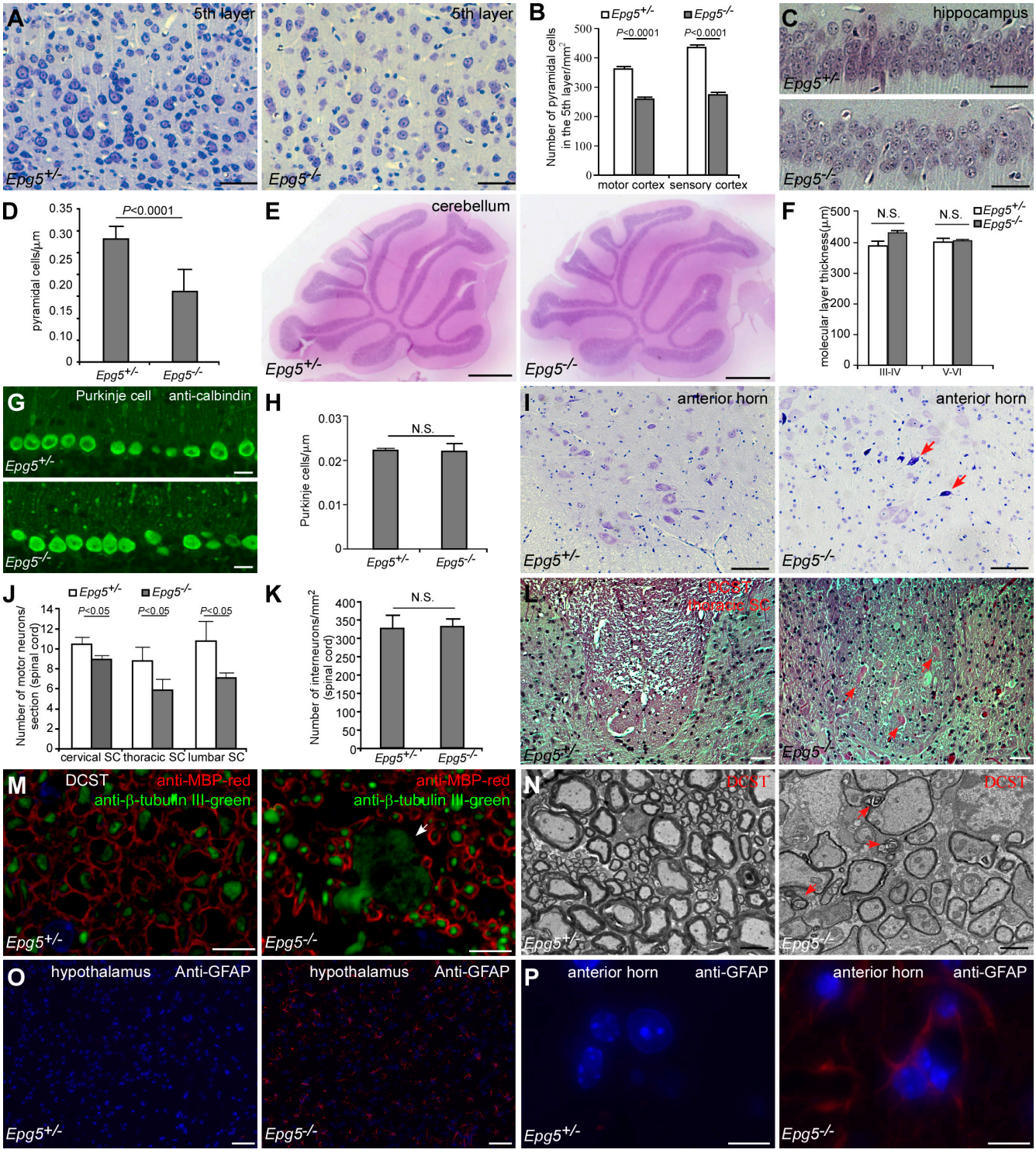

Figure 2. **Defects in brain and spinal cord in *Epg5*$^{-/-}$ mice.** (A) Nissl staining of the fifth layer of the cortex in 10-mo-old *Epg5*$^{+/-}$ and *Epg5*$^{-/-}$ mice. (B) The number of pyramidal cells in the fifth layer per millimeters squared. (C and D) H&E staining of the hippocampus shows reduced pyramidal cell numbers in *Epg5*$^{-/-}$ mice. Means ± SEM of three mice are shown in B and D. (E) The normally developed cerebellum in *Epg5*$^{-/-}$ mice. (F) The thickness of the molecular layer in the cerebellum in mutant and control mice. (G and H) Purkinje cells, stained by calbindin, are not reduced in number in *Epg5*$^{-/-}$ mice. Means ± SEM of five mice are shown in F and H. (I) Arrows indicate Pyknotic neurons in the anterior horn of *Epg5*$^{-/-}$ mice. (J) The number of motor neurons in the spinal cord (SC) in *Epg5*$^{+/-}$ and *Epg5*$^{-/-}$ mice. (K) The numbers of Nissl-stained interneurons in the spinal cord are similar in control and *Epg5*$^{-/-}$ mice. Means ± SEM of three mice are shown in J and K. (L) Eosinophilic spheroids (arrows) accumulate in the thoracic spinal cord of *Epg5*$^{-/-}$ mice. (M) Eosinophilic spheroids are swollen degenerating axons (arrow). (N) EM pictures showing degenerated axons (arrows) in the spinal cord of *Epg5*$^{-/-}$ mice. (O and P) GFAP staining in *Epg5*$^{+/-}$ and *Epg5*$^{-/-}$ mice. DCST, dorsal corticospinal tract. Bars: (A, C, L, and O) 50 μm; (E) 500 μm; (G) 20 μm; (I) 100 μm; (M and P) 10 μm; (N) 2 μm.

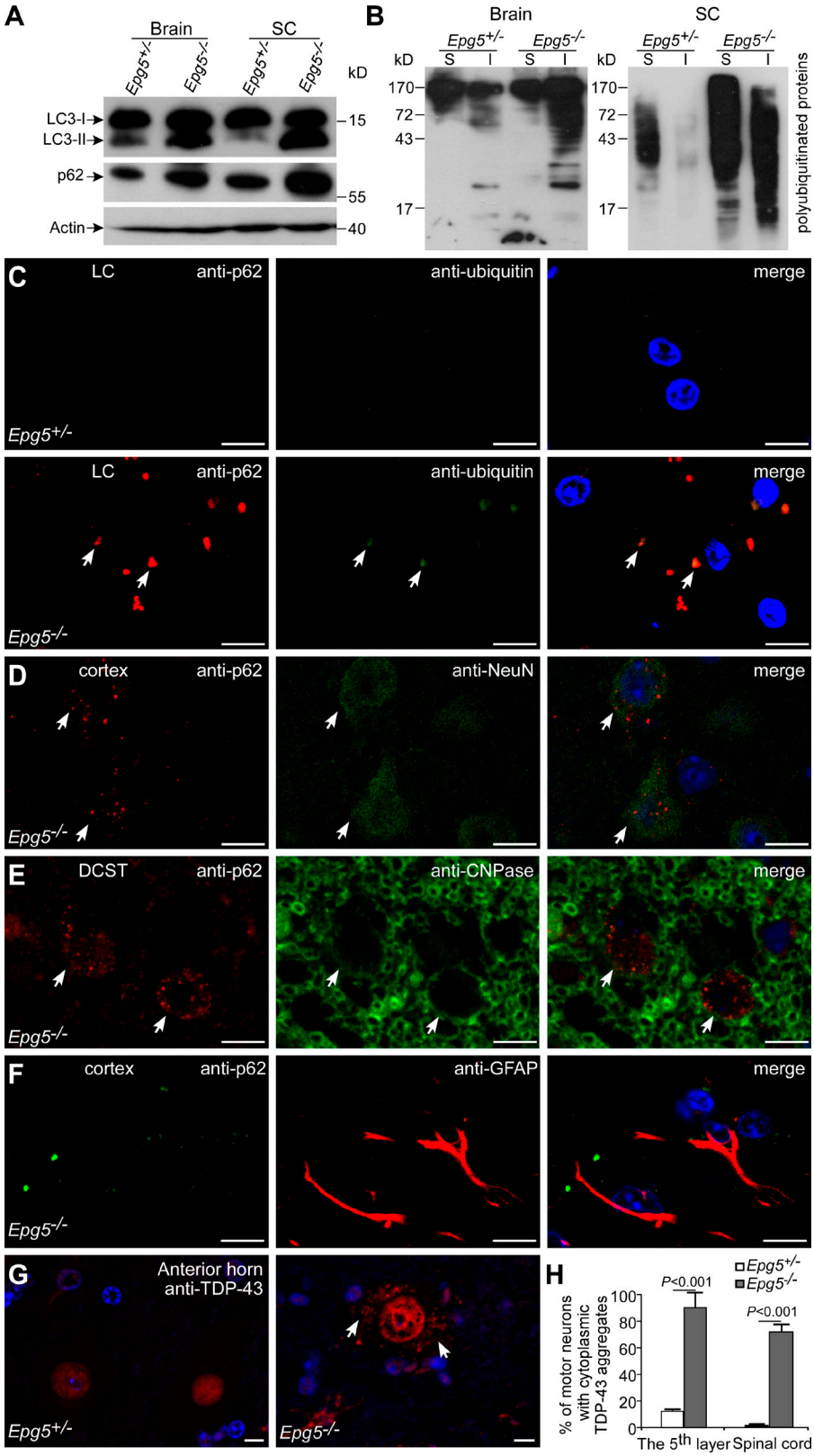

Figure 3. **Accumulation of LC3-II, p62 aggregates, and ubiquitin-positive inclusions in *Epg5* knockout mice.** (A) Levels of LC3 and p62 in brain and spinal cord extracts from $Epg5^{+/-}$ and $Epg5^{-/-}$ mice. SC, spinal cord. (B) Polyubiquitinated proteins in detergent-soluble (S) and -insoluble (I) fractions from brain and spinal cord homogenates of $Epg5^{+/-}$ and $Epg5^{-/-}$ mice. (C) p62 aggregates and ubiquitin-positive aggregates are absent from $Epg5^{+/-}$ mice but dramatically accumulate and are colocalized (arrows) in $Epg5^{-/-}$ mice. (D–F) p62 aggregates are detected in neurons (arrows; D) and oligodendrocytes (arrows; E) but absent from astrocytes (F) in $Epg5^{-/-}$ mice. (G) Cytoplasmic TDP-43 aggregates accumulate in motor neurons in the anterior horn of spinal cord in $Epg5^{-/-}$ mice. Arrows show cytoplasmic TDP-43 aggregates. DSCT, dorsal corticospinal tract. (H) Percentages of cytoplasmic TDP-43 aggregate-positive motor neurons in the fifth layer of cortex and anterior horn of the spinal cord in $Epg5^{+/-}$ and $Epg5^{-/-}$ mice. Means ± SEM of three mice are shown. LC, lateral column. Bars, 10 µm.

centrally nucleated fibers, vacuolated fibers, irregularly shaped atrophic fibers, and decreased myofiber size (Fig. 4, D–F). Consistent with this, the atrophy-related genes were up-regulated in $Epg5^{-/-}$ muscles (Fig. 4 G). Ultrastructurally, $Epg5^{-/-}$ muscles exhibited misaligned Z lines and accumulation of abnormal enlarged mitochondria (Fig. 4, H and I). Autophagic flux was also impaired in atrophic muscles (gastrocnemius myofibers) but not in adductor longus and vastus medialis of $Epg5^{-/-}$ mice (Figs. 4, J–L; and S2, D and E).

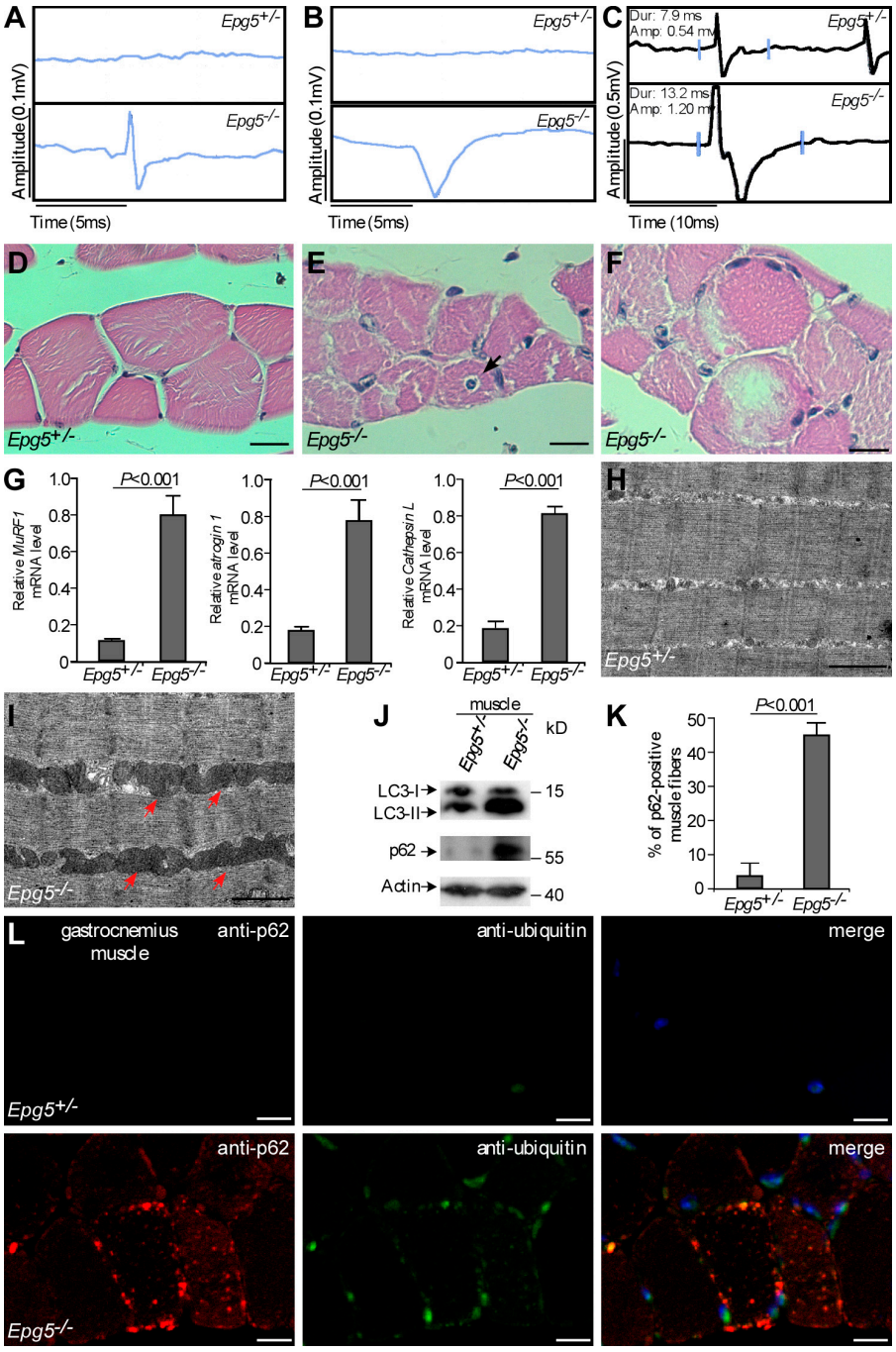

Figure 4. ***Epg5* knockout mice show muscle atrophy.** (A and B) Electromyography of the gastrocnemius muscle from a 3-mo-old *Epg5*$^{-/-}$ mouse showing fibrillations (A) and positive sharp waves (B). These defects were absent in control mice. (C) At 10 mo, *Epg5*$^{-/-}$ mice showed high-amplitude and long-duration action potentials when conducting MUAP tests. The blue lines show the start and end of an action potential. Dur, duration; Amp, amplitude. (D–F) H&E staining of gastrocnemius muscles showed features of muscle degeneration in *Epg5*$^{-/-}$ mice. The arrow in E indicates centrally nucleated fibers. (G) The transcription levels of the atrophy-related genes were up-regulated in gastrocnemius muscles of *Epg5*$^{-/-}$ mice. (H and I) Electron micrographs of *Epg5*$^{+/-}$ and *Epg5*$^{-/-}$ muscles. The arrows indicate abnormal enlarged mitochondria. (J) Levels of LC3-II and p62 in muscle extracts from *Epg5*$^{+/-}$ and *Epg5*$^{-/-}$ mice. (K) Percentage of p62 aggregate-positive myofibers in *Epg5*$^{+/-}$ and *Epg5*$^{-/-}$ mice. Means ± SEM of three mice are shown. (L) Accumulation and colocalization of p62 and ubiquitin aggregates in the gastrocnemius muscles of *Epg5*$^{-/-}$ mice but not controls. Bars: (D–F and L) 10 µm; (H and I) 1 µm.

Epg5$^{-/-}$ mice exhibit reduced adipose mass

Epg5$^{-/-}$ mice at 10–11 mo of age showed dramatic reduced mass of white adipose tissue. Wild-type adipocytes are morphologically homogeneous, and the entire cytoplasm is occupied by a single large unilocular lipid droplet (Fig. S2 F). However, mutant adipocytes were much smaller, and a large population of cells contained smaller multilocular lipid droplets (Fig. S2, C, F, and G). *Epg5*$^{-/-}$ livers at 10 mo appeared grossly normal, and the hepatic lobular structure was unchanged (Fig. S2 H). Levels of LC3-II and p62 were increased in *Epg5*$^{-/-}$ adipose tissues and liver fractions at 10 mo (Fig. S2 B), indicating that autophagic flux is impaired in these tissues.

Epg5 deficiency impairs autophagosome maturation

We further characterized the autophagy pathway in *Epg5*$^{-/-}$ primary mouse embryonic fibroblasts (MEFs). Under nutrient repletion conditions, LC3 puncta were largely absent from control MEFs but accumulated in *Epg5*$^{-/-}$ MEFs (Figs. 5, A and E; and S3, A–F). LC3-II levels were also elevated (Fig. 5 B). In control MEFs, the number of LC3 puncta dramatically increased 4 h after starvation and decreased 8 h after starvation, whereas in mutant MEFs, LC3 puncta continued to increase 8 h after starvation (Fig. 5, A and E; and S3, A–D). Upon bafilomycin A1 treatment, which inhibits lysosomal degradation, control MEFs showed increased LC3-II levels, whereas mutant

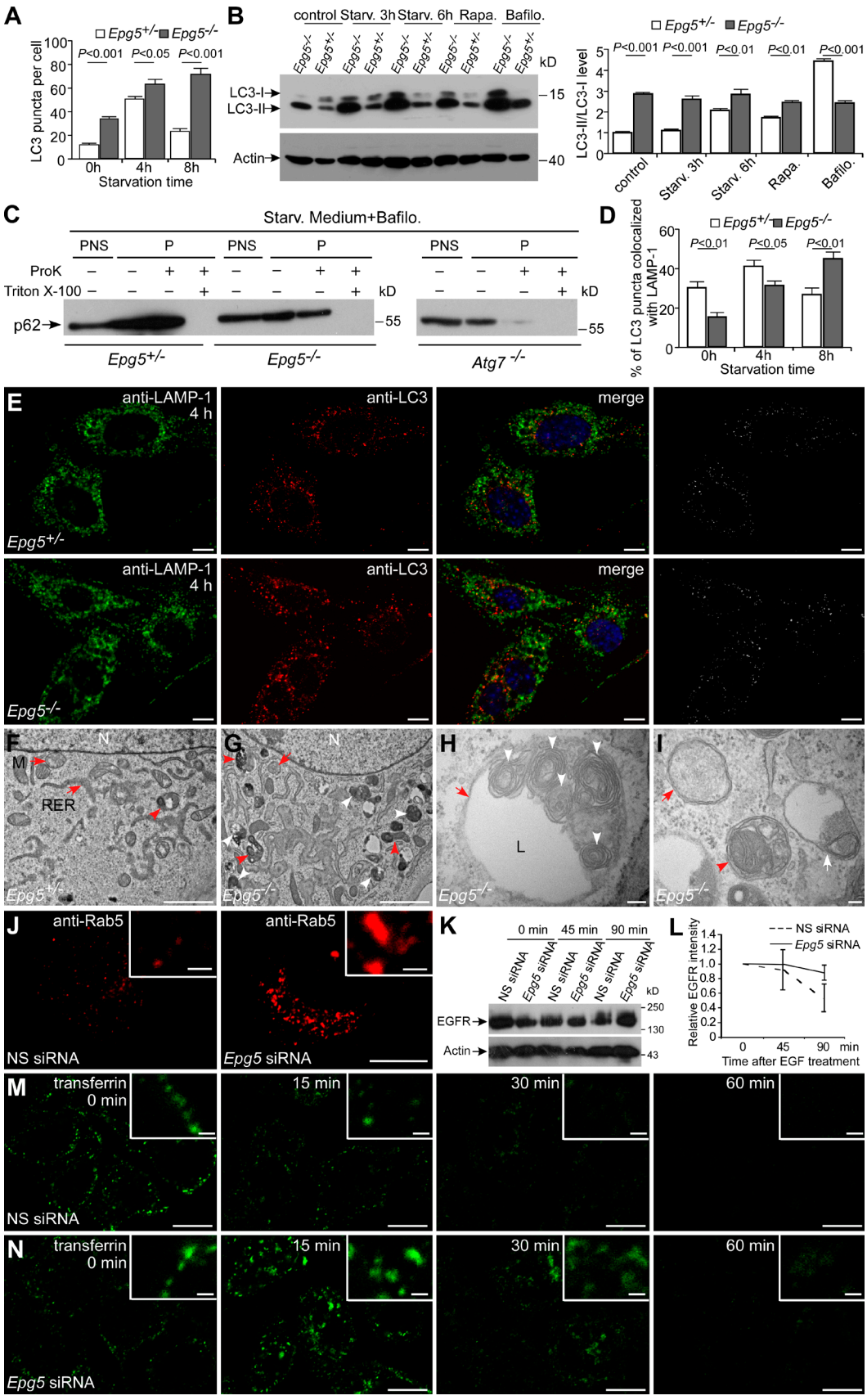

Figure 5. ***Epg5* deficiency causes a defect in autophagosome maturation and impairs endocytic trafficking.** (A) Number of LC3 puncta in *Epg5*$^{+/-}$ (control) and *Epg5*$^{-/-}$ MEFs. (B) Western blot showing levels of LC3-I and LC3-II in control and *Epg5*$^{-/-}$ MEFs upon indicated treatment (Starv., starvation; Rapa., rapamycin; Bafilo., bafilomycin A1). (C) Proteinase K (ProK) protection assay in different MEFs. PNS, postnuclear supernatant; P, pellet fractions. (D) Colocalization

MEFs exhibited no further elevation (Fig. 5 B), indicating that autophagic flux is impaired in *Epg5*$^{-/-}$ MEFs. Consistent with this, compared with control MEFs, *Epg5*$^{-/-}$ MEFs contained more p62 aggregates that largely colocalized with LC3 puncta (Fig. S3, E–H).

We performed a protease protection assay to determine whether autophagosome formation is completed in *Epg5*$^{-/-}$ MEFs. p62 sequestrated into autophagosomes is resistant to proteinase K digestion, whereas treatment with Triton X-100 permeabilizes the membrane, making p62 accessible to digestion (Velikkakath et al., 2012). After proteinase K treatment in the absence of Triton X-100, p62 was digested in *Atg7* (autophagosome defective) knockout MEFs but was protected in *Epg5*$^{-/-}$ and control MEFs, indicating that autophagosomes were sealed (Fig. 5 C). In control MEFs, the extensive colocalization of LC3 with LAMP-1– and LysoTracker-stained acidic lysosomes 4 h after starvation had decreased by 8 h, whereas in *Epg5*$^{-/-}$ MEFs, the colocalization continued to increase 8 h after starvation (Figs. 5, D and E; and S3, A–D, I, K, and L). p62 immunoreactivity also partially colocalized with LAMP-1–labeled structures in *Epg5*$^{-/-}$ MEFs (Fig. S3 J). However, lysosomal degradation of the self-quenched fluorophore DQ-BSA was much lower in *Epg5*$^{-/-}$ MEFs than control MEFs (Fig. S3, M and N). These results indicate that autophagosomes fuse with late endosomes/lysosomes in *Epg5*$^{-/-}$ MEFs, but the proteolysis activity of autolysosomes is greatly impaired.

No obvious autophagic structures were observed by EM in unstarved control MEFs (Fig. 5 F). However, *Epg5*$^{-/-}$ MEFs contained numerous autophagic vacuoles at all stages, including autophagosomes, possible amphisomes, and early autolysosomes (aAV-I [advanced autophagic vacuole type I], containing recognizable cytoplasmic content) or late autolysosomes (aAV-II, containing digested, unrecognizable content; Figs. 5, G–I; and S3 O). *Epg5*$^{-/-}$ MEFs had many complex vacuoles containing multiple membrane layers even under food repletion conditions (Fig. 5 H), suggesting that fusion of autophagosomes with lysosomes is hindered or the degradative activities of autolysosomes are impaired. After 4-h starvation, aAV-I and aAV-II autophagic vacuoles were increased in control and even more so in *Epg5*$^{-/-}$ MEFs (Fig. S3, P–S). Final-stage autolysosomal vacuoles (aAV-III), which contain a lipid-like area, were also detected in *Epg5*$^{-/-}$ MEFs under basal and starvation conditions (Figs. 5 I and S3, R and S), suggesting that autophagic degradation still proceeds slowly in *Epg5*-depleted cells.

Epg5 knockdown impairs endosomal trafficking

We next investigated the role of *Epg5* in the endocytic pathway. Compared with control cells, early endosomes and late endosomes were significantly enlarged in *Epg5* siRNA-treated cells (Figs. 5 J and S3 T). Degradation of EGF receptor (EGFR) was significantly slowed in *Epg5* siRNA-treated cells (Fig. 5, K and L), indicating that the endocytic degradation pathway is defective in *Epg5* knockdown cells. We further investigated endocytic recycling by following the transferrin transport, which is internalized into early endosomes and eventually returned to the surface and exported from the cell. In control cells, fluorescently conjugated transferrin was first localized on the plasma membrane, mostly recycled to the cell surface and released within 30 min, and completely disappeared after 1 h (Fig. 5 M). In *Epg5* siRNA-treated cells, internalized transferrin accumulated in the cytoplasm (Fig. 5 N), which partially colocalized with enlarged early and late endosomes but not with LysoTracker-stained acidified lysosomes (Fig. S3, V and W). After 30-min chasing, a large amount of transferrin was retained in the cytoplasm (Fig. 5 N). After l h, most transferrin was recycled to the surface and released (Fig. 5 N). These results indicate that loss of *Epg5* function slows endocytic degradation and delays endocytic recycling.

Conclusion

Here, we demonstrated that mice deficient in *Epg5* exhibit key features of ALS, including selective vulnerability of cortical layer 5 pyramidal neurons and spinal cord motor neurons, accumulation of cytoplasmic TDP-43 aggregates in motor neurons, progressive muscle weakness and atrophy, muscle denervation, and premature death. Although autophagy flux is systematically impaired and p62 aggregates accumulate in many regions of brain and spinal cord in *Epg5* knockout mice, only specific neuronal populations are degenerated. Selective neuronal damage in *Epg5* knockout mice is unlikely caused by the fact that motor neurons are more vulnerable to the autophagic defect. *Ei24* deficiency causes dramatically reduced interneurons, whereas motor neurons are largely normal, and there is no accumulation of eosinophilic spheroids in spinal cord (Zhao et al., 2012). The massive neuron degeneration in *Atg5*-, *Atg7*-, and *Ei24*-deficient mice could be caused by the fact that these genes have autophagy-independent function. For example, Atg5 and Atg7 also participate in cell secretion (DeSelm et al., 2011). Accumulation of nondegradative autophagic vacuoles may contribute to the pathogenesis of ALS in *Epg5*-deficient mice.

ratio of LC3 and LAMP-1 in control and *Epg5*$^{-/-}$ MEFs. 50 cells were examined per time point in A and D. (E) Colocalization of LC3 puncta and lysosomes in control and *Epg5*$^{-/-}$ MEFs 4 h after starvation. (F) Under nutrient repletion conditions, almost no autophagic elements are detected in *Epg5*$^{+/-}$ MEFs. RER, rough ER; M, mitochondrion; N, nucleus. The arrowhead indicates a vacuole with a late residual body-like appearance (aAV-III). (G) Under nutrient repletion conditions, *Epg5*$^{-/-}$ MEFs accumulate a large number of autophagic vacuoles. Red arrow, a likely autophagosome; red arrowheads, complex vacuoles of the aAV-I type; white arrowheads, aAV-II vacuoles. (H and I) High magnification of autophagic elements in unstarved *Epg5*$^{-/-}$ MEFs. (H) The red arrow indicates a complex autophagic vacuole containing multilayered membrane structures (white arrowheads) and a lipid-like region (L). (I) The red arrow indicates an autophagosome containing cytoplasm and ribosomes. The red arrowhead points to an autophagosome containing a mitochondrion and cytoplasmic material with membranous structures. The white arrow shows an aAV-III vacuole. (J) Compared with control cells, Rab5-labeled early endosomes are significantly enlarged in *Epg5* siRNA-treated cells. (K and L) EGFR degradation in control and *Epg5* knockdown cells. (M and N) Distribution of Alexa Fluor 488–conjugated transferrin at different time points in control siRNA- and *Epg5* siRNA-treated cells. Higher magnification views are shown in the insets. Error bars indicate SEMs. Bars: (E, J, M and N, main images) 10 µm; (F and G) 2 µm; (H and I) 100 nm; (J, M, and N, insets) 1 µm.

Functional impairment of the endosomal sorting complex required for transport or valosin-containing protein, which causes accumulation of nondegradative autophagic vacuoles, has been linked with familial ALS (Parkinson et al., 2006; Filimonenko et al., 2007; Lee et al., 2007; Ju et al., 2009; Johnson et al., 2010; Tresse et al., 2010). The ALS3 locus is mapped to chromosome 18q21, where *EPG5* is located (Hand et al., 2002). Our study implies that human *EPG5* might define an ALS susceptibility locus, and the animal model established here will help us to understand the molecular pathogenesis of ALS and to develop new therapeutic treatments.

Materials and methods

Generation of knockout mice

The *Epg5* targeting vector was constructed by substituting exons 18 and 19 of *Epg5* genomic DNA with a neomycin cassette. The Epg5 conventional knockout mice were generated in the National Institute of Biological Sciences Transgenic Research Center. The detailed procedure is as follows: After electroporation of the targeting vector into 129 R1 embryonic stem cells, colonies resistant to neomycin were chosen for homologous recombination by Southern blotting with probes 5′ and 3′ of the genomic sequence in the targeting vector. Heterozygous $Epg5^{+/-}$ embryonic stem cell clones were used to microinject C57BL/6N blastocysts. Chimeric offspring were mated with wild-type C57BL/6N mice. Heterozygotes from this cross were mated to obtain homozygous mutant mice. Germline transmission was confirmed by PCR analysis of tail DNA. The following primers were used to detect wild-type and deleted *Epg5* alleles: 5′-AGATAAGGTGTGTGACCCTTTGTG-3′ (forward wild-type allele), 5′-ATTGGGAAGACAATAGCAGGCATG-3′ (forward deleted allele), and 5′-TGTCTTACACAAGTGGTCCATGAG-3′ (reverse common). The expected sizes are 531 and 273 bp, respectively.

$Ei24^{flox/flox}$; nestin-*Cre* mice were on the C57BL/6N background, and exon 3 of *Ei24* was flanked by two loxP sequences. $Ei24^{flox/flox}$ mice were crossed with nestin-*Cre* to generate neural-specific *Ei24*-deficient mice. All mice were kept under specific pathogen-free conditions in the animal facility at the National Institute of Biological Sciences, Beijing. All animal experiments were approved by the institutional committee of the National Institute of Biological Sciences, Beijing.

Antibodies

The following antibodies were used: rabbit anti-p62 (PM045; MBL International), mouse anti-p62 (ab56416; Abcam), mouse antiubiquitin (3936; Cell Signaling Technology), rabbit anti-GFAP (bs-0199R; Bioss, Inc.), rabbit anti-LC3 (for Western blotting: PM046; MBL International), rabbit anti-LC3 (for immunostaining: 2775; Cell Signaling Technology), mouse anti–neuronal nuclei (MAB377; EMD Millipore), mouse anti–β-tubulin III (ab7751; Abcam), mouse anticalbindin (C9848; Sigma-Aldrich), mouse anti-CNPase (ab6319; Abcam), rabbit anti–myelin basic protein (ab40390; Abcam), rabbit anti–TDP-43 (12892–1-AP; Proteintech), rabbit antiperilipin (3470; Cell Signaling Technology), rabbit anti-Rab5 (3547; Cell Signaling Technology), rabbit anti-Rab7 (9367; Cell Signaling Technology), rabbit anti-EGFR (sc-03; Santa Cruz Biotechnology, Inc.), and mouse anti–β-actin (60008–1-Ig; Proteintech). Rabbit anti-Epg5 antibody was developed against a fragment of mouse Epg5 protein (amino acids 1,061–1,169).

Behavioral analysis

To monitor motor function, an accelerating rotarod (YLS-4C; Beijing Zhongshidichuang Science and Technology Development Co., Ltd) was used. After training for 2 d, mice were placed on the rolling rod with autoacceleration ranging from 5 to 20 rpm within 60 s for a maximum of 4 min. The time the animal stayed on the rod was measured.

Histology and immunohistochemistry

Mice were transcardially perfused with 10% neutral buffered formalin (Sigma-Aldrich). Tissues were postfixed and embedded in paraffin. For histological analysis, 5-µm sections were stained with hematoxylin and eosin (H&E) and examined by light microscopy (Imager.A1; Carl Zeiss) with a 40×/0.75 NA objective lens (Plan-Neofluar; Carl Zeiss) and a camera (AxioCam MRc 5; Carl Zeiss) used at RT. Images were processed and viewed using AxioVision 40 (v4.6.3.0; Carl Zeiss) software. For Nissl staining, sections were stained with 0.1% cresyl violet.

For immunohistochemical examination, sections were deparaffinized and rehydrated. Antigen retrieval was performed using the microwave method in 0.01 M citrate buffer for 10 min. After blocking, sections were incubated with primary antibodies overnight followed by a 1-h incubation with FITC or rhodamine-labeled secondary antibodies (Jackson ImmunoResearch Laboratories, Inc.) and counterstained with DAPI (Vector Laboratories). Finally, fluorescence was detected under an epifluorescence microscope or a confocal microscope (LSM 510 Meta plus Axiovert zoom; Carl Zeiss) with 63×/1.40 NA oil immersion objective lens (Plan-Apochromat; Carl Zeiss) and a camera (AxioCam HRm; Carl Zeiss) at RT. Images were processed and viewed using LSM Image Browser software. Sections of the lumbar spinal cord were stained in this study unless otherwise noted.

Cell counting

To count the number of spinal cord motor neurons, fixed spinal cords were sequentially sectioned at 5 µm, and every sixth section was stained with 0.1% cresyl violet. Neurons meeting the following criteria were scored as motor neurons: (a) with a distinct nucleus; (b) with a diameter of ≥25 µm; and (c) located in the anterior horn ventral to the line tangential to the ventral tip of the central canal. To examine cortical neurons, large pyramidal cells located in the fifth layer of the motor and sensory cortices were quantified. The number of pyramidal cells in the hippocampus was quantified and divided by the length of this layer. The number of Purkinje cells in lobules III, IV, and V were quantified and divided by the total length of the lobules. The thickness of the molecular layer was measured as the distance between lobule III and IV or lobule V and VI, divided by 2.

Protein extraction and Western blotting

Total proteins from mouse tissues were extracted with radioimmunoprecipitation assay buffer (50 mM Tris-HCl, pH 7.4, 150 mM NaCl, 1 mM EDTA, 0.1% SDS, and 1% NP-40) supplemented with 1 mM PMSF and protease inhibitor cocktail (Roche). Protein concentrations were determined by Bradford protein assay (GenStar Biosolutions). Equal amounts (30–40 µg) of proteins were separated by SDS-PAGE electrophoresis and transferred onto a polyvinylidene fluoride membrane. After incubation with primary and secondary antibodies, the immunoreactivity of the membrane was detected using an ECL kit (Thermo Fisher Scientific). Results are representative of at least three experiments.

To prepare detergent-soluble and -insoluble fractions, mouse tissues were homogenized in 5 vol sucrose buffer (0.25 M sucrose, 50 mM Tris-HCl, pH 7.4, and 1 mM EDTA) supplemented with 1 mM PMSF and protease inhibitors. The supernatants were collected after centrifuging at 2,500 rpm for 10 min at 4°C, and the protein concentration was adjusted to 4 µg/µl. An aliquot of 100 µl supernatant was lysed with an equal volume of sucrose buffer containing 1% Triton X-100 and then centrifuged at 15,000 rpm for 15 min at 4°C. The resulting supernatants were used as a detergent-soluble fraction. Pellets were dissolved in 200 µl of 1% SDS in PBS (detergent-insoluble fraction).

Quantitative RT-PCR

Total RNA from mice tissues was extracted using TRIZOL (Invitrogen), and cDNA was synthesized by SuperScript III First-Strand kit (Invitrogen). Quantitative PCR was performed on a cycler (Mastercycler ep Realplex 4; Eppendorf) using SYBR Premix Ex Taq (Takara Bio Inc.). Data were normalized to the *actin* level. Results are representative of at least three experiments. The following primers were used: *p62* forward, 5′-GCTGCCCTATACCCACATCT-3′; *p62* reverse, 5′-CGCCTTCATCCGAGAAAC-3′; *MuRF1* forward, 5′-ACCTGCTGGTGGAAAACATC-3′; *MuRF1* reverse, 5′-CTTCGTGTTCCTTGCACATC-3′; *atrogin 1* forward, 5′-GCAAACACTGCCACATTCTCTC-3′; *atrogin 1* reverse, 5′-CTTGAGGGGAAAGTGAGACG-3′; *Cathepsin L* forward, 5′-GTGGACTGTTCTCACGCTCAAG-3′; *Cathepsin L* reverse, 5′-TCCGTCCTTCGCTTCATAGG-3′; *actin* forward, 5′-CTGGCTCCTAGCACCATGAAGAT-3′; and *actin* reverse, 5′-GGTGGACAGTGAGGCCAGGAT-3′.

Proteasome activity assay

To determine proteasome activity, aminomethylcoumarin (AMC)-linked synthetic peptide substrates were used: Ac-Gly-Pro-Leu-Asp-AMC, Suc-Leu-Leu-Val-Tyr-AMC, and Ac-Arg-Leu-Arg-AMC (and Boc-Leu-Arg-Arg-AMC) for caspase-like, chymotrypsin-like, or trypsin-like activity, respectively (Proteasome Substrate Pack; Enzo Life Sciences). Mouse tissues were homogenized in lysis buffer (50 mM Hepes, pH 7.5, 5 mM EDTA, 150 mM NaCl, 1% Triton X-100, and 2 mM ATP). The protein concentration of the lysate was adjusted to 8 µg/µl. An aliquot of 250 µl lysate was incubated

with 2.5 µl of each substrate (final concentration of 50 nM) for 30 min at 37°C in the dark. After adding 252.5 µl of precooled 96% ethanol solution to stop the reaction, proteasome activity of the mixture was measured by detecting fluorescence from AMC hydrolysis (380-nm excitation and 460-nm emission).

Transmission EM

Mice were perfused with 2% PFA/2% glutaraldehyde. Tissues were dissected and postfixed in 2.5% glutaraldehyde followed by fixation in 1% OsO_4 for 2 h. After dehydration with graded ethanol solutions, tissues were embedded in EMbed812 (Electron Microscopy Sciences). 80-nm ultrathin sections were stained with 2% uranyl acetate for 30 min and lead citrate for 10 min.

Cells were fixed with 2% PFA and 0.25% glutaraldehyde in PBS, pH 7.4, at 37°C for 2 h and then dehydrated in a graded ethanol series and embedded. 70-nm ultrathin sections were mounted, stained, and dried at RT. The samples were visualized using a 120-kV electron microscope (H-7650B; Hitachi) at 80 kV, and images were captured by a charge-coupled device camera (XR-41; Advanced Microscopy Techniques) using DigitalMicrograph software (Gatan, Inc.) at RT.

Cell culture, transfection, and immunostaining

Primary MEFs generated from day 13.5 embryos from *Epg5*$^{+/-}$ crosses or HeLa cells were cultured in DMEM supplemented with 10% FBS, 100 U/ml penicillin, 100 µg/ml streptomycin, and 2 mM glutamine. *Epg5* siRNA and nonsense (NS) siRNA were purchased from GenePharma. The sequences were as follows: NS siRNA, 5′-UUCUCCGAACGUGUCACGUTT-3′; and *Epg5* siRNA, 5′- GAACAGGUGUACCCAAGCU-3′. Cells were transfected with siRNAs using Lipofectamine 2000 (Invitrogen) for 72 h according to the manufacturer's instructions.

For immunostaining, cells were plated on glass-bottomed dishes. After overnight recovery, cells were starved in serum-free medium for the indicated time. Cells were washed with PBS, fixed in 4% PFA for 10 min, and permeabilized in cold methanol for 10 min. After blocking with 10% FBS in PBS for 30 min at RT, cells were incubated with antibodies overnight at 4°C, washed with PBS three times, and then stained with fluorescently labeled secondary antibodies. Coverslips were mounted on microscope slides with mounting medium with DAPI. Images were acquired with a confocal microscope (LSM 510 Meta). Dot numbers were analyzed by ImageJ software (National Institutes of Health), and colocalization masks and ratios were analyzed by Imaris software (Bitplane).

DQ-BSA degradation assay

72 h after transfection with *Epg5* siRNA or NS siRNA, cells were serum starved for 2 h and then treated with 10 µg/ml DQ-BSA (Life Technologies/Invitrogen) for 30 min. Cells were then washed with PBS, fixed, permeabilized, and stained with DAPI. The fluorescent signal from lysosomal proteolysis of DQ-BSA was recorded by confocal microscope (LSM 510 Meta).

Transferrin recycling

Cells were cultured in 3.5-cm dishes with a 1-cm microwell and transfected with NS siRNA or *Epg5* siRNA. 72 h after transfection, 0.1 mg/ml Alexa Fluor 488–conjugated transferrin (Invitrogen) was added into each plate and incubated for 30 min on ice. Cells were washed with PBS and incubated with regular medium at 37°C for the indicated times before transferrin distribution was examined.

For examining the colocalization of transferrin with various endosome compartments, LC3 puncta, and p62 aggregates, cells transfected with *Epg5* siRNA or NS siRNA were incubated with 0.1 mg/ml Alexa Fluor 488–conjugated transferrin in regular medium for 1 h at 37°C. Then, the cells were fixed, permeabilized, and incubated with anti-Rab5, -Rab7, -LC3, or -p62 antibodies and secondary antibodies.

EGFR degradation assay

Control and *Epg5* siRNA-treated HeLa cells were serum starved overnight and treated with 100 ng/ml EGF and 25 µg/ml cycloheximide for the indicated period. Cells were then washed with PBS and lysed. Degradation of EGFR was examined using an immunoblotting assay with the anti-EGFR antibody.

Protease protection assay

Cultured MEF cells were starved, treated with bafilomycin A1, harvested, and suspended in homogenization buffer (20 mM Hepes-KOH, pH 7.4, 0.22 M mannitol, 0.07 M sucrose, and protease inhibitors). *Atg7* knockout MEFs were provided by M. Komatsu (Tokyo Metropolitan Institute of Medical Science, Setagaya-ku, Tokyo, Japan). Cells were then passed 10 times through a 27-gauge needle using a 1-ml syringe and centrifuged at 2,000 rpm for 5 min. The supernatant (as postnuclear supernatant) was centrifuged again at 10,000 rpm to obtain the pellet fraction. The pellet was resuspended in homogenization buffer and then treated with 100 µg/ml proteinase K with or without 0.5% Triton X-100. After 20-min incubation on ice, 10% TCA was added, and the samples were centrifuged at 10,000 rpm for 5 min. The pellet (as pellet fraction) was washed with ice-cold acetone, resuspended in SDS-PAGE sample buffer, and boiled immediately. Proteinase K digestion was detected by Western blotting.

Electromyography

Evoked CMAP, MUAP, and resting potentials were evaluated with an electromyogram apparatus (Keypoint; Dantec) and analyzed by software (Keypoint.NET; Dantec). For evaluating CMAP, we stimulated the sciatic nerve at the tuberosity of the ischium by a single 0.1-ms, 1-Hz, and 20-mA supramaximal pulse and recorded CMAPs from the medial part of the gastrocnemius with a 26-guage concentric needle electrode (37 × 0.46 mm, recording area of 0.07 mm^2; Alpine). The MUAP of the gastrocnemius and bicipital muscles was recorded with the same type of needle electrode from a single motor unit at moderate contractions. Resting potentials were recorded with the same needle electrode.

Statistical analysis

Data from at least three sets of samples were used for statistical analysis. Statistical significance was calculated by Student's *t* test. $P < 0.05$ was considered significant.

Online supplemental material

Fig. S1 shows defects in the brain and spinal cord in *Epg5*$^{-/-}$ mice. Fig. S2 shows muscle atrophy in *Epg5*-deficient mice. Fig. S3 shows a defect in the maturation of autophagosomes into degradative autolysosomes in *Epg5*$^{-/-}$ MEFs. Online supplemental material is available at http://www.jcb.org/cgi/content/full/jcb.201211014/DC1.

We are grateful to Dr. Zelda Cheung for helpful comments on the manuscript, Dr. Masaaki Komatsu for *Atg7* MEFs, the National Institute of Biological Sciences Transgenic Research Center for generating *Epg5* conventional knockout mice, and Dr. Isabel Hanson for editing work.

This work was supported by the National Basic Research Program of China (2013CB910100 and 2011CB910100) to H. Zhang and Hungarian Scientific Research Funds (OTKA K75843) to A.L. Kovács. The research of H. Zhang was supported in part by an International Early Career Scientist grant from the Howard Hughes Medical Institute.

Submitted: 2 November 2012
Accepted: 12 February 2013

References

Boillée, S., C. Vande Velde, and D.W. Cleveland. 2006. ALS: a disease of motor neurons and their nonneuronal neighbors. *Neuron*. 52:39–59. http://dx.doi.org/10.1016/j.neuron.2006.09.018

DeSelm, C.J., B.C. Miller, W. Zou, W.L. Beatty, E. van Meel, Y. Takahata, J. Klumperman, S.A. Tooze, S.L. Teitelbaum, and H.W. Virgin. 2011. Autophagy proteins regulate the secretory component of osteoclastic bone resorption. *Dev. Cell*. 21:966–974. http://dx.doi.org/10.1016/j.devcel.2011.08.016

Ferraiuolo, L., J. Kirby, A.J. Grierson, M. Sendtner, and P.J. Shaw. 2011. Molecular pathways of motor neuron injury in amyotrophic lateral sclerosis. *Nat. Rev. Neurol*. 7:616–630. http://dx.doi.org/10.1038/nrneurol.2011.152

Filimonenko, M., S. Stuffers, C. Raiborg, A. Yamamoto, L. Malerød, E.M. Fisher, A. Isaacs, A. Brech, H. Stenmark, and A. Simonsen. 2007. Functional multivesicular bodies are required for autophagic clearance of protein aggregates associated with neurodegenerative disease. *J. Cell Biol.* 179:485–500. http://dx.doi.org/10.1083/jcb.200702115

Hand, C.K., J. Khoris, F. Salachas, F. Gros-Louis, A.A. Lopes, V. Mayeux-Portas, C.G. Brewer, R.H. Brown Jr., V. Meininger, W. Camu, and G.A. Rouleau. 2002. A novel locus for familial amyotrophic lateral sclerosis, on chromosome 18q. *Am. J. Hum. Genet.* 70:251–256. http://dx.doi.org/10.1086/337945

Hara, T., K. Nakamura, M. Matsui, A. Yamamoto, Y. Nakahara, R. Suzuki-Migishima, M. Yokoyama, K. Mishima, I. Saito, H. Okano, and N. Mizushima. 2006. Suppression of basal autophagy in neural cells causes neurodegenerative disease in mice. *Nature*. 441:885–889. http://dx.doi.org/10.1038/nature04724

Hardy, J., and K. Gwinn-Hardy. 1998. Genetic classification of primary neurodegenerative disease. *Science*. 282:1075–1079. http://dx.doi.org/10.1126/science.282.5391.1075

Johnson, J.O., J. Mandrioli, M. Benatar, Y. Abramzon, V.M. Van Deerlin, J.Q. Trojanowski, J.R. Gibbs, M. Brunetti, S. Gronka, J. Wuu, et al; ITALSGEN Consortium. 2010. Exome sequencing reveals VCP mutations as a cause of familial ALS. *Neuron*. 68:857–864. http://dx.doi.org/10.1016/j.neuron.2010.11.036

Ju, J.S., R.A. Fuentealba, S.E. Miller, E. Jackson, D. Piwnica-Worms, R.H. Baloh, and C.C. Weihl. 2009. Valosin-containing protein (VCP) is required for autophagy and is disrupted in VCP disease. *J. Cell Biol.* 187:875–888. http://dx.doi.org/10.1083/jcb.200908115

Komatsu, M., S. Waguri, T. Chiba, S. Murata, J. Iwata, I. Tanida, T. Ueno, M. Koike, Y. Uchiyama, E. Kominami, and K. Tanaka. 2006. Loss of autophagy in the central nervous system causes neurodegeneration in mice. *Nature*. 441:880–884. http://dx.doi.org/10.1038/nature04723

Lee, J.A., A. Beigneux, S.T. Ahmad, S.G. Young, and F.B. Gao. 2007. ESCRT-III dysfunction causes autophagosome accumulation and neurodegeneration. *Curr. Biol.* 17:1561–1567. http://dx.doi.org/10.1016/j.cub.2007.07.029

Levine, B., and G. Kroemer. 2008. Autophagy in the pathogenesis of disease. *Cell*. 132:27–42. http://dx.doi.org/10.1016/j.cell.2007.12.018

Longatti, A., and S.A. Tooze. 2009. Vesicular trafficking and autophagosome formation. *Cell Death Differ.* 16:956–965. http://dx.doi.org/10.1038/cdd.2009.39

Lu, Q., P.G. Yang, X.X. Huang, W.Q. Hu, B. Guo, F. Wu, L. Lin, A.L. Kovács, L. Yu, and H. Zhang. 2011. The WD40 repeat PtdIns(3)P-binding protein EPG-6 regulates progression of omegasomes to autophagosomes. *Dev. Cell*. 21:343–357. http://dx.doi.org/10.1016/j.devcel.2011.06.024

Mizushima, N., T. Yoshimori, and B. Levine. 2010. Methods in mammalian autophagy research. *Cell*. 140:313–326. http://dx.doi.org/10.1016/j.cell.2010.01.028

Nakatogawa, H., K. Suzuki, Y. Kamada, and Y. Ohsumi. 2009. Dynamics and diversity in autophagy mechanisms: lessons from yeast. *Nat. Rev. Mol. Cell Biol.* 10:458–467. http://dx.doi.org/10.1038/nrm2708

Neumann, M., D.M. Sampathu, L.K. Kwong, A.C. Truax, M.C. Micsenyi, T.T. Chou, J. Bruce, T. Schuck, M. Grossman, C.M. Clark, et al. 2006. Ubiquitinated TDP-43 in frontotemporal lobar degeneration and amyotrophic lateral sclerosis. *Science*. 314:130–133. http://dx.doi.org/10.1126/science.1134108

Otomo, A., L. Pan, and S. Hadano. 2012. Dysregulation of the autophagy-endolysosomal system in amyotrophic lateral sclerosis and related motor neuron diseases. *Neurol. Res. Int.* 2012:498428.

Parkinson, N., P.G. Ince, M.O. Smith, R. Highley, G. Skibinski, P.M. Andersen, K.E. Morrison, H.S. Pall, O. Hardiman, J. Collinge, et al; MRC Proteomics in ALS Study; FReJA Consortium. 2006. ALS phenotypes with mutations in CHMP2B (charged multivesicular body protein 2B). *Neurology*. 67:1074–1077. http://dx.doi.org/10.1212/01.wnl.0000231510.89311.8b

Pasinelli, P., and R.H. Brown. 2006. Molecular biology of amyotrophic lateral sclerosis: insights from genetics. *Nat. Rev. Neurosci.* 7:710–723. http://dx.doi.org/10.1038/nrn1971

Tian, Y., Z.P. Li, W.Q. Hu, H.Y. Ren, E. Tian, Y. Zhao, Q. Lu, X.X. Huang, P.G. Yang, X. Li, et al. 2010. *C. elegans* screen identifies autophagy genes specific to multicellular organisms. *Cell*. 141:1042–1055. http://dx.doi.org/10.1016/j.cell.2010.04.034

Tresse, E., F.A. Salomons, J. Vesa, L.C. Bott, V. Kimonis, T.P. Yao, N.P. Dantuma, and J.P. Taylor. 2010. VCP/p97 is essential for maturation of ubiquitin-containing autophagosomes and this function is impaired by mutations that cause IBMPFD. *Autophagy*. 6:217–227. http://dx.doi.org/10.4161/auto.6.2.11014

Velikkakath, A.K., T. Nishimura, E. Oita, N. Ishihara, and N. Mizushima. 2012. Mammalian Atg2 proteins are essential for autophagosome formation and important for regulation of size and distribution of lipid droplets. *Mol. Biol. Cell*. 23:896–909. http://dx.doi.org/10.1091/mbc.E11-09-0785

Zhang, X., L. Li, S. Chen, D. Yang, Y. Wang, X. Zhang, Z. Wang, and W. Le. 2011. Rapamycin treatment augments motor neuron degeneration in SOD1(G93A) mouse model of amyotrophic lateral sclerosis. *Autophagy*. 7:412–425. http://dx.doi.org/10.4161/auto.7.4.14541

Zhao, Y.G., H. Zhao, L. Miao, L. Wang, F. Sun, and H. Zhang. 2012. The p53-induced gene Ei24 is an essential component of the basal autophagy pathway. *J. Biol. Chem.* 287:42053–42063. http://dx.doi.org/10.1074/jbc.M112.415968